

Coupled plastic strain- and stress-induced phase transformations and microstructure evolution in Fe-7%Mn alloy in dynamic rotational diamond anvil cell

Sorb Yesudhas^{1*}, Mrinmay Sahu¹, Valery I. Levitas^{1,2*}, Dean Smith³, and Jeffrey T. Lloyd⁴

¹Department of Aerospace Engineering, Iowa State University, Ames, Iowa 50011, USA

²Department of Mechanical Engineering, Iowa State University, Ames, Iowa 50011, USA

³HPCAT, X-ray Science Division, Argonne National Laboratory, Argonne, Illinois 60439, USA

⁴Armor Mechanisms Branch, DEVCOM Army Research Laboratory, Aberdeen Proving Ground, Maryland 21005, USA

*Corresponding authors. Email: sorbya@iastate.edu, vlevitas@iastate.edu

Abstract

The first experiments in dynamic rotational diamond anvil cell (dRDAC) on severe plastic deformation (SPD) and BCC \leftrightarrow HCP phase transformation (PT) at pressure up to 27.6 GPa, rotation rates up to 1,500 RPM, and strain rates up to 2,094 /s are performed considering Fe-7%Mn alloy as an example. The BCC-HCP PT initiates at 11.4 GPa under hydrostatic loading while it is 3.2 GPa under plastic compression. Strong effect of plastic straining leads to unique kinetics with simultaneous direct and reverse PTs, not studied for any material. For quasi-static loading, parameters in the kinetics for the strain-induced direct-reverse PTs and stationary volume fraction versus pressure are found. During torsion with 1,000 and 1,500 RPM, volume fraction of the HCP phase does not change. After torsion stops, it increases by 30% within a few minutes after 1,000 RPM and HCP phase disappears after 1,500 RPM. These findings contradict general wisdom that strain-induced PTs occur only during straining, time is not a governing parameter, and kinetics is determined by plastic strain instead of time. Thus, nuclei of the HCP phase are generated during straining at high strain rate, but growth/disappearance occur under stresses at much longer time scales. Consequently, a new theory of combined strain- and stress-induced PTs is required. The following important rule is revealed: crystallite size of ~ 30 nm, microstrain ~ 0.004 , and dislocation density $\sim 1.1 \times 10^{15}/\text{m}^2$ in the HCP phase are steady during static compression and dynamic torsion, during and after the PT and after torsion. These parameters are independent of pressure,

plastic strain tensor, its path, strain rates, and volume fraction of the HCP phase. Obtained results open fundamental research on combined strain- and stress-induced PTs and microstructure evolution under dynamic SPD and high pressure.

Introduction

PTs that occur during severe plastic deformations (SPD) under high pressure play a very important role in physical and material experiments [1-3], synthesis of high-pressure phases [1-5] and nanostructured materials [6,7], bulk and surface processing (cutting, polishing, lapping) of materials [8,9], friction, military applications [10], and interpretation of geological behavior, and phenomena like deep-focus earthquakes [11,12]. It was revealed that plastic deformations reduce the PT by one to two orders of magnitude compared to hydrostatic loading, enables obtaining and stabilization of novel high-pressure phases, and often reveals entirely new transformation pathways [1-5,13-15]. For their analysis and theoretical description, a concept of plastic strain-induced PTs was introduced in [16,17]. Traditional temperature-, pressure, and stress-induced PTs start predominantly at pre-existing defects (various dislocation configurations, stacking faults, disclinations, etc.), which produce a concentration of stress tensor and nucleation sites. For stress-induced PTs, applied stresses are below the yield strength. Due to limited number of pre-existing defects, one must increase pressure/stresses and/or change temperature to activate nucleation at defects with weaker stress concentrations. PTs caused by plastic flow are coined as plastic strain-induced or strain-induced PTs. They occur by nucleating at new defects permanently generated during plastic flow. The only defect which can reduce the PT pressure by one to two orders of magnitude is the dislocation pileup. It possesses the largest concentration of all components of the stress tensor at its tip proportional to the number of dislocations in a pileup, which can be 10 and even 100. The strain-induced PTs represent a separate class of PTs that require a completely different thermodynamic and kinetic description as well as experimental characterization. Dislocation pileup-based nucleation mechanism was confirmed by analytical [16,17], phase-field [18,19], and atomistic [20,21] approaches, as well as experimentally [3], see reviews [13-15].

Compression in a diamond anvil cell (DAC) and especially torsion in rotational DAC (RDAC) represent the methods for in situ studies of strain-induced PTs [2,3,5,13-15], in contrast to ex situ studies with high-pressure torsion (HPT) with metallic/ceramic anvils [4,6,7,22]. It is generally accepted that for strain-induced PTs, the volume fraction of the high-pressure phase

(HPP) is a growing function of the plastic strain; when the straining stops, PTs stop as well [2,4,13-17]. Therefore, time is not an essential parameter; instead, plastic strain plays the role of a time-like parameter. The first general kinetic equation for strain-induced PTs based on this assumption was derived in [16,17] utilizing the accumulative plastic strain q as a time-like parameter. It has been experimentally confirmed in [22,23] and further advanced via coupled experimental computational method in [24] for irreversible α - ω PT in Zr only. Also, rules for microstructure (crystallite size and dislocation density) evolution during SPD and PTs and mutual effects of the microstructure and PTs were found in situ for Zr [25,26] and Si [3]. All these RDAC studies have been performed under slow quasi-static loading; in HPT, the maximum achieved strain rate was 20 /s [27] but without in situ capabilities.

However, there are practical and fundamental needs to study processes in RDAC for high strain rates, up to 10^4 /s. Many applications, like military (armor penetration, shock propagation and mitigation [10]), dynamic material synthesis, ball milling, fast velocity friction and wear, deep-focus earthquake initiation [11,12], meteorite impact, etc. require understanding material behavior under high-strain rate SPD and PT. Fundamental questions are whether strain rate and time affect the strain-induced PT and microstructure evolution and how; what are the new rules, and whether new theories are required? To address these problems, we developed dRDAC with rotation speed up to 4,000 RPM and used it for strain rates up to 2,094 /s, pressure up to 27.6 GPa and SPD. None of other dynamic methods, like drop-weight impact, dynamic DAC, Kolsky/Hopkinson bars, plate, pressure-shear plate, or laser impacts, shock wave, Z-machine, etc., can provide SPD under high pressure in this range of parameters along with detailed in situ probing of the occurring processes. In addition, since temperature does not change during deformation due to the high thermal conductivity of diamonds and small sample thickness, the strain rate effects are decoupled from temperature, which is impossible to accomplish with other techniques.

The Fe-7%Mn alloy was chosen as the first material for testing because of its importance for shock mitigation strategies [10] and unique transformational and deformational properties. It undergoes reversible BCC-HCP PT, and the effect of plastic straining on both PTs is strong, so both direct-and reverse PTs occur simultaneously until steady volume fraction of the high-pressure phase is reached, different for different pressures. The kinetics of such a PT is expected to be much different from the kinetics for irreversible strain-induced PTs [16,17], but was never studied quantitatively in experiments for any material.

Experimental Details

The Fe-7%Mn alloy with properties described in [10] was supplied by Army Research Laboratory. The initial dimension of the sample was 36.8 mm \times 25.7 mm \times 14.9 mm. The sample thickness of 14.9 mm was reduced to approximately 5 mm by cutting it into three pieces using electrical discharge machining (EDM) at the Ames National Laboratory machine shop. The sample thickness was further reduced to 280 μ m by cross rolling using the 100T rolling mill in the same machine shop to produce nanograined structure. For dynamic shear experiments, we have used dRDAC from DAC Tools, LLC, IL. We have used a pair of diamonds with culet size of 300 μ m and roughened surfaces with asperity of \sim 400 nm (instead of traditional 10 nm) prepared for us by lapping by Almax Easy Lab to increase the contact friction stress to the maximum possible one equal to the yield strength in shear. Two samples with the thickness of 280 μ m were punched out with the diameter of 5 mm using the punch and die set. These samples were pre-indented to thicknesses of 168 μ m and 159 μ m and were used for run 1 and run 2 cycles respectively for the dynamic shear measurements. No pressure transmitting media were used for these experiments. The high-pressure compression and shear time resolved X-ray diffraction (XRD) experiments were performed at the 16-ID-B beam line, HPCAT, utilizing Advanced Photon Source with X-ray wavelengths 0.4246 Å. The XRD measurements were carried out using PILATUS3 X 2M CdTe detector with the X-ray beam focused on the sample to a spot size of 1.3 μ m \times 1.9 μ m. The samples were compressed in dRDAC using membrane. Time profiles for shear were designed in DT Move software (DAC Tools, LLC), and the driving motor (CPM-SCHP-2346P-ELSA) of the dRDAC was triggered by the PILATUS3 detector *via* a delay generator (Berkeley Nucleonic model 505) to ensure synchronization of XRD collection and shear. The minimum data collection time for time resolved X-ray diffraction and absorption measurements was 5 ms. The data were collected along the sample diameter with a step size of 10 μ m. Thus, for 10 and 100 RPM, we scanned along the sample diameter during the real-time XRD experiments, i.e., along the spiral for a twisted sample. Before and after each torsion, data were collected along the sample diameter. The 2D XRD images were converted to the intensity vs. 2theta profile using diopbase software [28], and were post processed using Materials Analysis Using Diffraction (MAUD) to calculate the lattice parameters, volume fractions, crystallite size, and microstrain by the Rietveld refinement method [29].

Experimental results

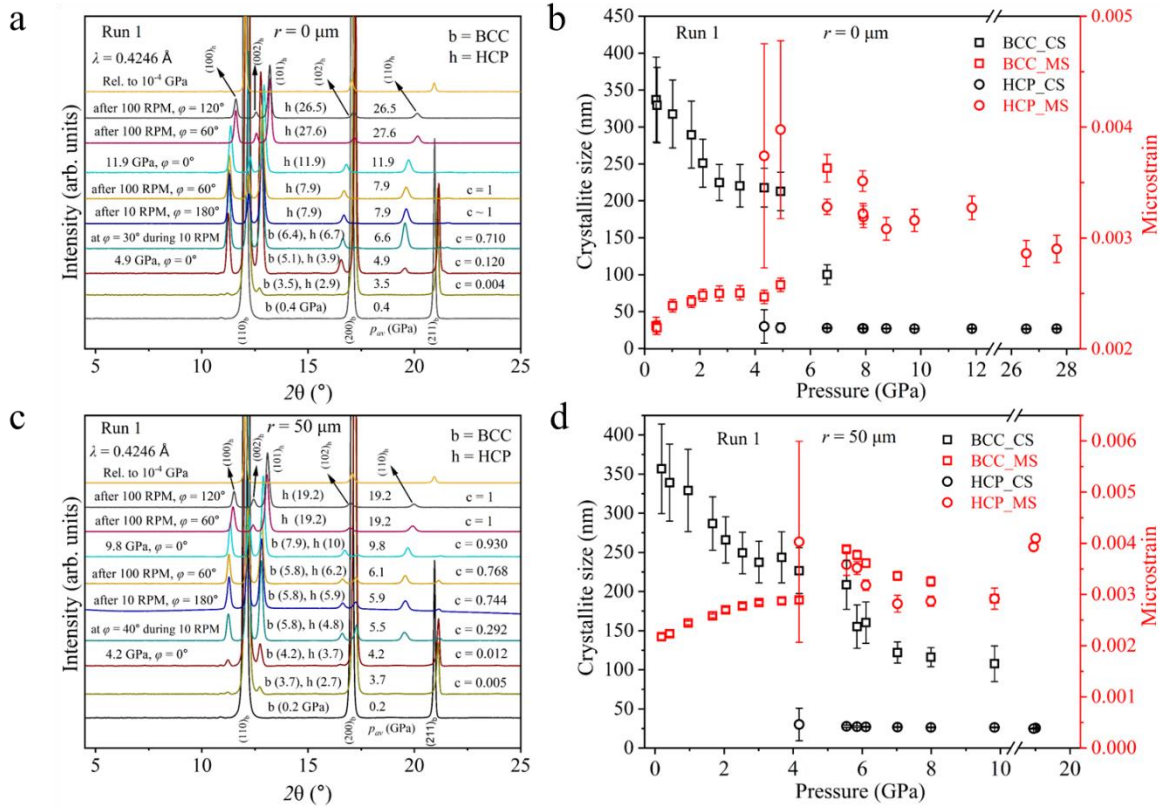


Fig. 1. High pressure XRD patterns and microstructure evolution of Fe-7%Mn alloy collected during and after compression and torsion in dRDAC with different rotation rates in run 1. (a) and (c) XRD patterns at $r = 0$ and $r = 50 \mu\text{m}$, and (b) and (d) the microstructure evolution at $r = 0$ and $r = 50 \mu\text{m}$. Compression-torsion program, including rotation rate in RPM and rotation angle (φ) for the corresponding rotation rates are shown on the left side. In the next column, the pressures in the BCC (b) and HCP (h) phases are shown in parentheses. The average pressure (p_{av}) shown at the middle right column. The volume fractions of each phase are presented in the rightmost column.

Under hydrostatic loading, the BCC-HCP PT initiates at 11.4 GPa and completes at 15.9 GPa. Under plastic compression, the minimum pressure at which BCC-HCP PT starts is 3.2 GPa, i.e., the effect of plastic straining on the PT pressure is quite strong. For comparison, for Fe, PT initiation pressure is 14.9-15.5 GPa under hydrostatic loading and 10.9 GPa during torsion in RDAC [30].

The Figs. 1 and 2 exhibit the evolution of high-pressure phases and their crystallite size and microstrain under compression and shear at the sample center, $r = 0 \mu\text{m}$, and at the radius $r = 50 \mu\text{m}$ for runs 1 and 2. In run 1, the sample was initially compressed to 4.9 GPa, resulting in a volume fraction, $c = 0.12$ at $r = 0 \mu\text{m}$ (Fig. 1a). The initiation of the HCP phase at $r = 0 \mu\text{m}$ is noticed by the appearance of two shoulder peaks, $(100)_h$ and $(101)_h$, on either side of the $(110)_b$ peak of the BCC phase at 3.5 GPa, which is 3.7 GPa at $r = 50 \mu\text{m}$ (Figs. 1a and c). A 180° shear

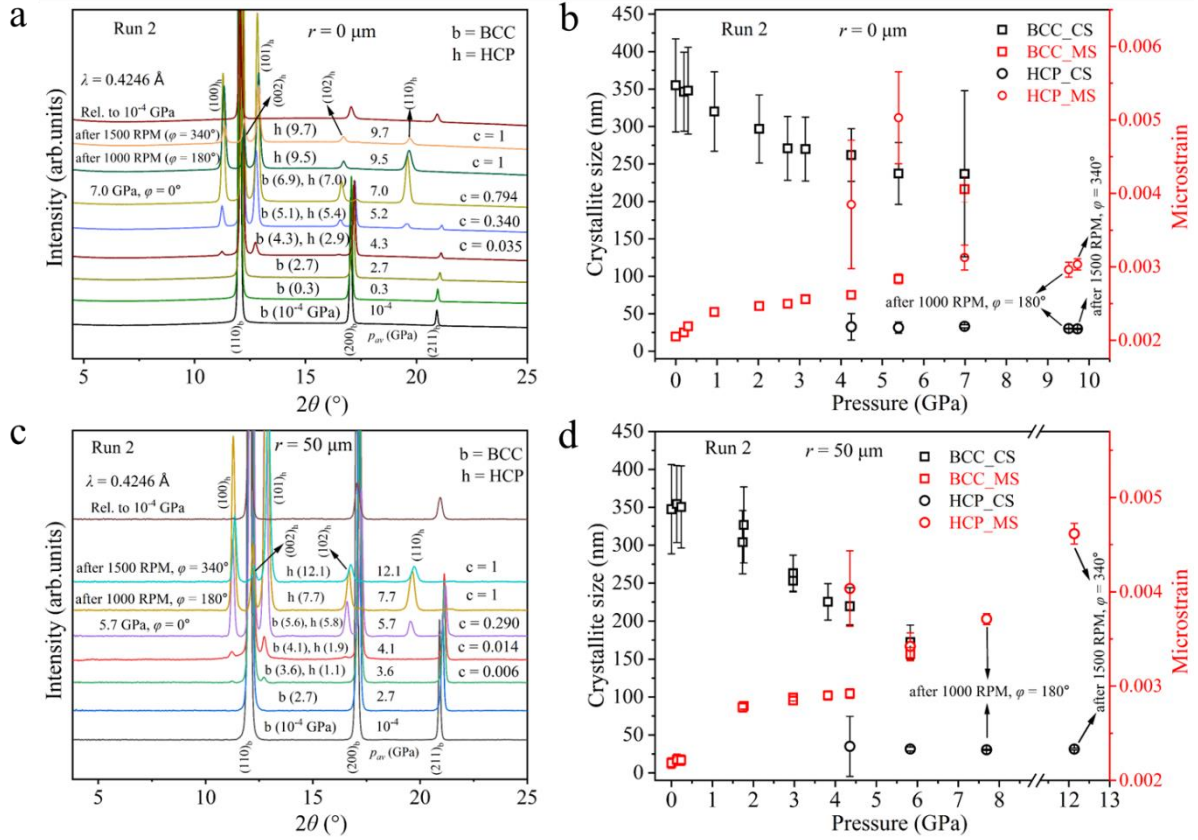


Fig. 2. High pressure XRD patterns and microstructure evolution of Fe-7%Mn alloy collected during and after compression and torsion in dRDAC with different rotation rates for run 2. (a) and (c) HPXRD at $r = 0$ and $r = 50 \mu\text{m}$ for run 2, and (b) and (d) the crystallite size and microstrain evolution at $r = 0$ and $r = 50 \mu\text{m}$. Compression-torsion program, including rotation rate in RPM and rotation angle φ for the corresponding rotation rates are shown on the left side. In the next column, the pressures in the BCC (b) and HCP (h) phases are shown in parentheses. The volume fractions of each phase are presented in the rightmost column.

was then applied at an anvil speed of 10 RPM with 4.9 GPa at $r = 0 \mu\text{m}$. For the 10 RPM experiment, time-resolved XRD data were collected along the sample diameter. During torsion with 10 RPM by 400, the average pressure over both phases, p_{av} , at $r = 50 \mu\text{m}$ increased from 4.2 to 5.5 GPa, accompanied by an increase in the volume fraction of HCP phase from 0.012 to 0.292 (Fig. 1c). But at $r = 0 \mu\text{m}$, the volume fraction drastically increased from 0.12 to 0.71 for rotation angle $\phi = 300$ and p_{av} increased from 4.9 to 6.6 GPa. After $\phi = 1800$, at $r = 50 \mu\text{m}$, p_{av} increased to 5.9 GPa and $c = 0.744$, while at the center, p_{av} increased to 7.9 GPa and PT is practically completed.

The XRD data collected along the sample diameter after shear ($\phi = 1800$) indicate that the pressure in the BCC phase remains almost constant with further shearing, and the pressure slightly increased from 5.8 to ~ 5.85 GPa for $\phi = 300$ at 100 RPM in time at each point at $r = 50 \mu\text{m}$, whereas that in the HCP phase increased by 1.1 GPa, getting practically equal to pressure in the parent phase at $r = 50 \mu\text{m}$ whereas a significant pressure increase observed in both phases at $r = 0 \mu\text{m}$ (Figs. 1a, c). That means that large plastic shear eliminates internal pressure difference between phases that appear due to transformation strain. The initiation of BCC-HCP PT observed at 3.2 GPa, $r = 40 \mu\text{m}$ (3.5 GPa at $r = 0 \mu\text{m}$).

Subsequently, a 60° shear was applied at an anvil speed of 100 RPM at 7.9 GPa. At $r = 0 \mu\text{m}$, no change in pressure and c is noticed (Fig. 1a). Interestingly, the pressure in the BCC phase at $r = 50 \mu\text{m}$ remains constant, while that in the HCP phase increases by 0.3 GPa, along with 2.5 % increase in its volume fraction. The sample was compressed further to 11.9 GPa at $r = 0 \mu\text{m}$. As a result, the average pressure in the sample is increased to 9.8 GPa at $r = 50 \mu\text{m}$, and the pressure in HCP phase is seen to be 2.1 GPa larger than that in BCC phase (Fig. 1c). Also, the volume fraction of HCP increases to 0.93, which is evidenced by the reduction in the intensity of the $(200)_b$ peak of the BCC phase. At 11.9 GPa, at $r = 0 \mu\text{m}$, the sample was again sheared by 60° at 100 RPM, resulting in a significant pressure increase from 11.9 GPa to 27.6 GPa (Fig. 1a). At $r = 50 \mu\text{m}$, the BCC-HCP PT completed and the pressure is increased from 9.8 to 19.2 GPa (Fig. 1c). Upon applying an additional 120° shear at 100 RPM, the pressure at $r = 0 \mu\text{m}$ is dropped by 0.9 GPa, while the pressure remains constant at $r = 50 \mu\text{m}$. Time-resolved XRD measurements were conducted at $r = 0 \mu\text{m}$ for all the 100 RPM shear experiments at 7.9, 11.9 and 27.6 GPa at $r = 0 \mu\text{m}$. A reverse HCP-to-BCC is initiated at 4.5 GPa evidenced by the emergence of $(200)_b$ peak of BCC phase, and the HCP phase completely transforms to BCC at 1.4 GPa.

In Run 2, the sample was initially compressed to 7 GPa in seven steps, exhibiting an 0.794 volume fraction of the HCP phase at $r = 0 \mu\text{m}$ (Fig. 2a). At $r = 50 \mu\text{m}$, the pressure and volume fraction for the same compression stage are 5.7 GPa, and 0.29, respectively (Fig. 2c). The initiation of BCC-HCP PT is seen at 4.3 GPa at $r = 0 \mu\text{m}$ and 3.6 GPa at $r = 50 \mu\text{m}$ (Fig. 2c). At 4.3 GPa, the pressure in the BCC phase is 1.4 GPa higher than that in the HCP phase at $r = 0 \mu\text{m}$ whereas it is 2.5 GPa higher at $r = 50 \mu\text{m}$ (Fig. 2a, c). After applying a 180° shear at an anvil speed of 1,000 RPM at 7 GPa, the BCC phase completely transforms into the HCP phase at $r = 0 \mu\text{m}$ and $r = 50 \mu\text{m}$, with the pressure increase to 9.5 GPa and 7.7 GP at these points, respectively. When the

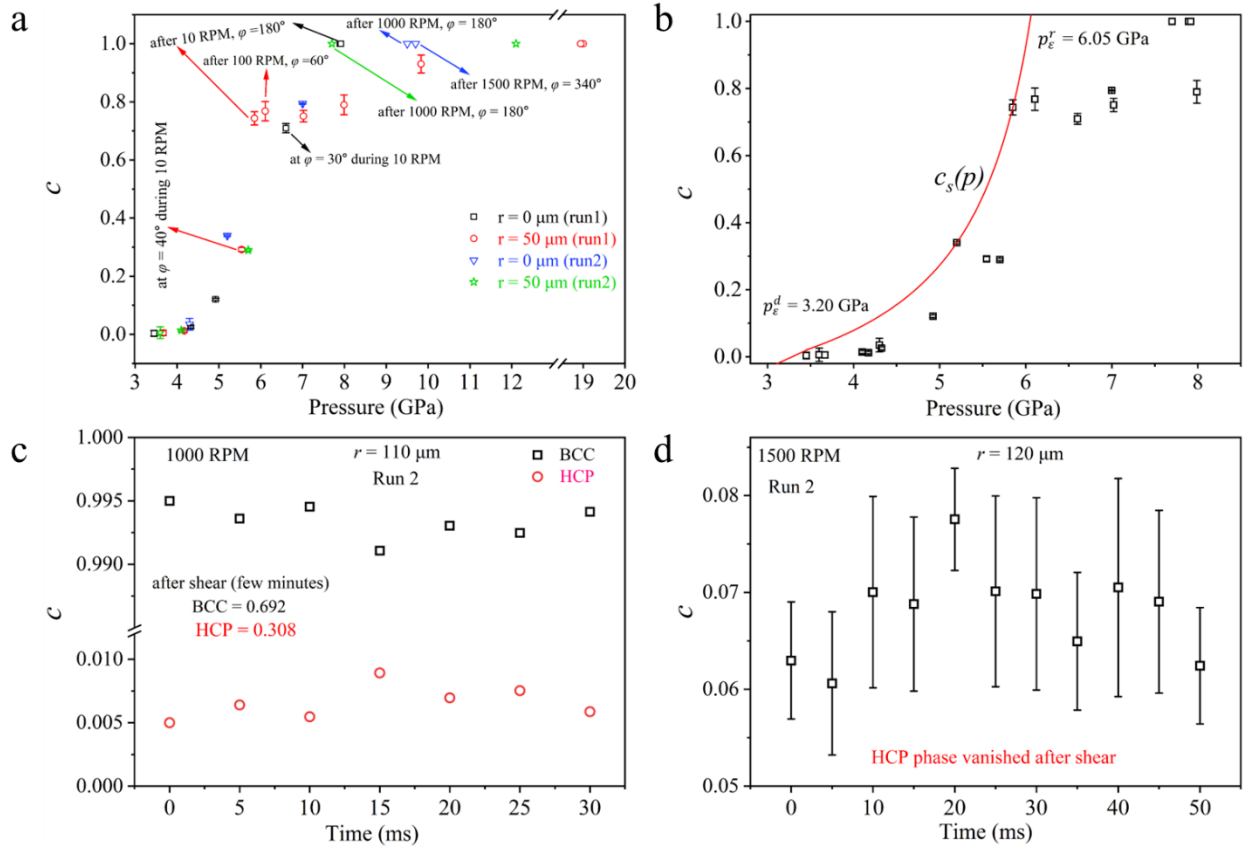


Fig. 3. Evolution of the volume fraction (c) of phases for different compression-torsion loadings before, during and after shear at different radii, r . (a) At $r = 0 \mu\text{m}$ and $r = 50 \mu\text{m}$ for run 1 and 2 after compression, and torsion with different rotation rates as function of pressure. (b) The same data for smaller pressure range and theoretical curve (red) for the steady volume fraction of the HCP phase $c_s(p)$ from Eq. (2) fitted to the three points with maximum c for each pressure. (c) Time resolved volume fraction evolution of BCC and HCP phases with 5 ms step size at $r =$

110 μm , 1000 RPM, and at 7 GPa at $r = 0 \mu\text{m}$. **(d)** Time resolved volume fraction evolution of HCP phase with 5 ms step size at $r = 120 \mu\text{m}$, 1500 RPM, and at 9.5 GPa at $r = 0 \mu\text{m}$.

sample was subsequently sheared by 340° at 1500 RPM, only a slight pressure increases 0.2 GPa at $r = 0 \mu\text{m}$ but a noticeable pressure increases by 4.4 GPa seen at $r = 50 \mu\text{m}$. Time-resolved XRD data were collected at $r = 110 \mu\text{m}$ and $r = 120 \mu\text{m}$ during the 1000 RPM and 1500 RPM, respectively. After 1500 RPM, the pressure in HCP phase at $r = 50 \mu\text{m}$ is 2.4 GPa higher than that at $r = 0 \mu\text{m}$.

Figs. 1b, d and 2b, d show the evolution of crystallite size (CS) and microstrain (MS) for the BCC and HCP phases of Fe-7%Mn. The evolution of CS and MS shows opposite trends until the onset of the phase transformation. Since the XRD peaks of the HCP phase are too weak at the onset of the phase transformation, the CS and MS values at the initiation point are not reported. The maximum change in the crystallite size of the HCP phase is approximately 5 nm in Run 1.

Figs. 3a and b present most of the typical experimental points from both runs in terms of c versus p_{av} in different pressure ranges. These data will be used below for the connection with the theory and determination of the steady state volume fraction $c_s(p)$ (red line in Fig. 3b) and some material parameters in the kinetic equation for strain-induced PT,

For time-resolved data in Fig. 3 (c), during torsion with 1,000 RPM at $r = 110 \mu\text{m}$, pressure is 3.5 GPa in BCC phase and 3.8 GPa in HCP phase before torsion and practically did not change during torsion. Volume fraction of HCP phase varied in narrow range $c = 0.005\text{-}0.009$, i.e. PT practically did not occur during the torsion. Surprisingly, c increased to 0.31 after a few minutes after torsion stops at 4.1 GPa (bcc) and 4.5 GPa (hcp). During the following torsion with 1,500 RPM at $r = 120 \mu\text{m}$, pressure is 3.45 GPa in BCC phase and 3.51 GPa in HCP phase before torsion and practically did not change during torsion (Fig. 3d). Volume fraction of HCP phase varied in narrow range of 0.060-0.077. After torsion stopped, $p = 3.9$ GPa, and the HCP phase disappeared after a few minutes.

During compression, the crystallite size in BCC phase reduced from 355 nm to 237 nm at 7 GPa at $r = 0 \mu\text{m}$ and to 172 nm at 5.8 GPa at $r = 50 \mu\text{m}$ (Fig. 2b, d). Crystallite size in the HCP phase is ~ 30 nm from the beginning of its nucleation, during following static compression for both

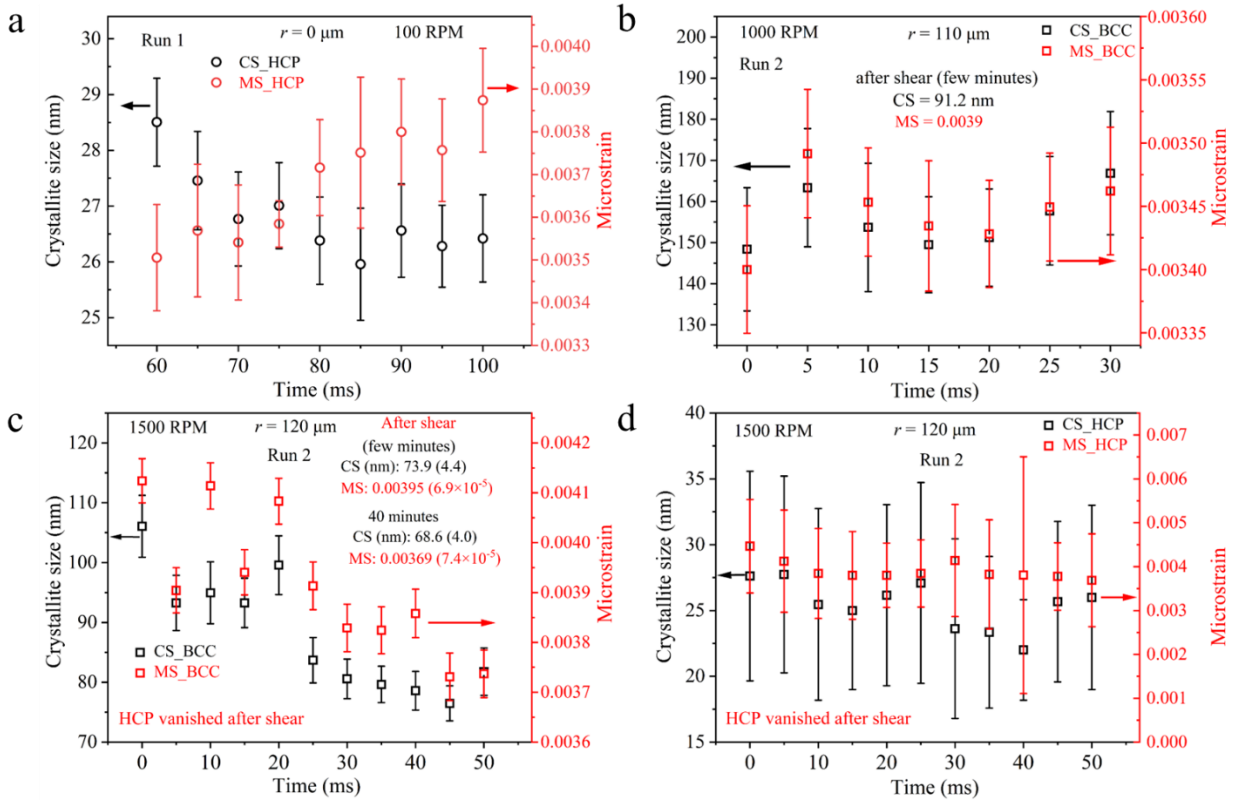


Fig. 4. Time resolved XRD study of crystallite size and microstrain evolution in BCC and HCP phases during the same compression-torsion loadings as in Fig. 3c and d, and for 100 RPM at $r = 0$. (a) Microstructure evolution in HCP phase at $r = 0 \mu\text{m}$ for 100 RPM. (b) Microstructure evolution in BCC phase at $r = 110 \mu\text{m}$ for 1000 RPM. (c) Microstructure evolution in BCC phase at $r = 120 \mu\text{m}$ for 1500 RPM. (d) Microstructure evolution in HCP phase at $r = 120 \mu\text{m}$ for 1500 RPM. Each time resolved data were collected with a step size of 5 ms.

sample radii, torsion with 1,000 and 1,500 RPM, and after each of these torsions (Figs. 2b, d and, 4d). The microstrain in the HCP phase is also practically constant during these processes and equal to ~ 0.004 . Since the dislocation density in the Rietveld refinement procedure [1,2] is determined in terms of crystallite size and microstrain, it also remains constant in the HCP phase. Using simplified equation for the dislocation density $\rho_d = \frac{1}{d^2}$, we obtain $\rho_d = 1.1 \times 10^{15}/\text{m}^2$.

Time resolved evolution of the crystallite size and microstrain in BCC phase during the same loadings as in Fig. 4d is presented in Fig. 4b and c. For 1,000 RPM, the crystallite size first

increases from 148 nm to 163 nm during acceleration stage, then reduces to 151 nm and then increases again to 167 nm during deceleration to zero rotation speed. The microstrain for this case also increases from 0.00340 to 0.00349 during acceleration then reduces to 0.00343 and then increases again to 0.00346 during deceleration to zero rotation speed. They change to 91 nm and 0.0039 after a few minutes after torsion stops. After the reverse PT and full pressure release, the crystallite size of BCC iron is ~ 100 nm. For 1,500 RPM (Fig. 4c), the crystallite size in BCC phase decreases from 106 nm to a steady ~ 82 nm. The microstrain reduces from 0.00412 to 0.00373. After torsion stops, they change to 74 nm and 0.00395 after a few minutes and to 69 nm and 0.00369 after 40 minutes.

Discussion

Phase transformation

Quasi-static kinetics. According to theory in [16,17], when both direct and reverse PTs occur simultaneously, the kinetic equation for the strain-induced PT is

$$\frac{dc}{dq} = \frac{k_d(1-c)}{c\left(\frac{\sigma_{y1}}{\sigma_{y2}}\right)+(1-c)} \left(\frac{p-p_\epsilon^d}{p_h^d-p_\epsilon^d}\right) H(p-p_\epsilon^d) - \frac{k_r c}{c+(1-c)\left(\frac{\sigma_{y2}}{\sigma_{y1}}\right)} \left(\frac{p_\epsilon^r-p}{p_\epsilon^r-p_h^r}\right) H(p_\epsilon^r-p). \quad (1)$$

Here, p_ϵ^d and p_ϵ^r are the minimum pressure for direct and maximum pressure for the reverse strain-induced PTs, respectively; p_h^d and p_h^r are the minimum pressure for direct and maximum pressure for the reverse pressure-induced PTs, respectively; the Heaviside unit step function H ($H(x) = 1$ for $x \geq 0$; $H(x) = 0$ for $x < 0$) ensures that the term for the direct PT contributes at $p > p_\epsilon^d$ only, and the term for the reverse PT is nonzero for $p < p_\epsilon^r$; k_d and k_r are the kinetic coefficients for direct and reverse PTs, respectively; q is the accumulated plastic strain, and σ_{y2} and σ_{y1} are the yield strengths of the high- and low-pressure phases, respectively. Eq. (1) is derived utilizing results from the nanoscale mechanism of the strain-induced nucleation at the tip of the dislocation pileup [16,17]. Since edge dislocation pileups generate both compressive and tensile stresses of the same magnitude in different regions, they promote simultaneously direct and reverse PTs in different regions. Therefore, Eq. (1) has terms for direct and reverse PTs. Eq. (1) is independent of time; plastic strain q is the time-like parameter.

In the pressure range $p_\epsilon^d \leq p \leq p_\epsilon^r$, Eq. (1) has a stationary solution

$$c_s = \frac{1}{1+M\frac{(1-\tilde{p})}{\tilde{p}}}; \quad \tilde{p} = \frac{p-p_\varepsilon^d}{p_\varepsilon^r-p_\varepsilon^d}; \quad M = \left(\frac{\sigma_{y1}}{\sigma_{y2}}\right) \left(\frac{k_r}{k_d}\right) \frac{(p_h^d-p_\varepsilon^d)}{(p_h^d-p_\varepsilon^r)}, \quad (2)$$

which can be reached for large enough plastic strain; it is an increasing function of pressure; $c_s(p_\varepsilon^d) = 0$ and $c_s(p_\varepsilon^r) = 1$. For $p > p_\varepsilon^r$ and $p < p_\varepsilon^d$, complete direct and reverse PTs can be reached in a steady state. While Eq. (1) for the absent reverse PT was calibrated for $\alpha \rightarrow \omega$ PT in Zr [22-24], the case with simultaneous direct and reverse PTs was not considered for any material.

In Fig. 3a and b, all experimental points for different plastic strains are placed in the p - c plane. Points with maximum c for each p can be considered a low bound for the steady $c_s(p)$, see red line in Fig. 3b. One point in this line, $p_\varepsilon^d = 3.20$ GPa, with $c_s(p_\varepsilon^d) = 0$, was determined directly from experiment. Eq. (2) for $c_s(p)$ has two more material parameters, p_ε^r and M . They are determined from the condition that the plot $c_s(p)$ passes through two other points with maximum c for all pressures (Fig. 3b). This leads to $p_\varepsilon^r = 6.05$ GPa and $M = 4.57$. Note that these parameters were not previously known for any material.

Analysis of Eq. (2) shows that for $M = 1$, $c_s(M = 1) = \tilde{p}$, which can be considered as equal promotion of direct and reverse PTs. Since c_s is a decreasing function of M , obtained $M = 4.57$ means that the reverse PT is promoted more than the direct one. With known M , let us evaluate material parameters affecting it. Taking for iron $\sigma_{y1} = 1.1$ GPa and $\sigma_{y2} = 3$ GPa [31] and assuming that the modest effect of Mn on the strength Fe [10] does not change the ratio σ_{y1}/σ_{y2} for iron, we obtain $\sigma_{y1}/\sigma_{y2} = 0.367 < 1$. Such a value smaller than 1 promotes direct PT by localizing applied plastic strain in a weaker lower-pressure phase.

For $p_\varepsilon^d = 3.20$ GPa, $p_\varepsilon^r = 6.05$ GPa, $p_h^d = 11.4$ GPa, and $p_h^r = 4.5$ GPa, $\frac{p_h^d-p_\varepsilon^d}{p_\varepsilon^r-p_h^r} = 5.29 > 1$, i.e., this parameter promotes reverse PT. While it looks counterintuitive that larger effect of the plastic straining on PT pressures $p_h^d - p_\varepsilon^d$ for direct PT than $p_\varepsilon^r - p_h^r$ for the reverse promotes the kinetics of the reverse PT, this also follows from Eq. (1), where these differences are in denominators for the corresponding PT terms. With these values and $M = 4.57$, one obtains $\frac{k_r}{k_d} = 2.35$, which makes an additional contribution for promotion of the reverse PT compared to the direct PT. That is why essential volume fraction of the HCP phase can be obtained at pressure essentially higher than p_ε^d only. Thus, all but one (e.g., k_d or k_r) parameters in the kinetic Eq. (1) are estimated; special design

of experiment is required to complete the kinetic model. Since the fastest experiment for which data for c_s were used was at 10 RPM and small $r = 50 \mu\text{m}$, obtained kinetic parameters characterize quasi-static loading.

Need for time-dependence of the kinetic for strain-induced PT. The main surprise is that PT practically does not occur during fast torsion with 1,000 and 1,500 RPM, but c increases by 0.30 after torsion with 1,000 RPM and reduces by 0.07 down to zero after torsion with 1,500 RPM within a few minutes. These results challenge the traditional wisdom that kinetics of strain-induced PTs is independent of time and depends on plastic strain only as a time-like parameter. Theoretically, this statement was justified in [16,17] as follows. Nucleation of the high-pressure phase at the tip of the dislocation pileup is barrierless and occurs at ps to ns time scale. Growth away from the tip is very limited because all stresses strongly reduce with distance from the tip. Usually, it occurs till steady state during the time much shorter than the measurement time; therefore, only steady states are detected, which depend on plastic strain only and are independent of time. Here, due to much faster deformation, smaller time resolution, and low pressure, time-dependent growth at constant plastic strain is revealed. Thus, HCP nuclei are generated during straining at high strain rate, but their growth/disappearance till steady state occurs at the few minute time scales. Since growth occurs at constant plastic strain, it represents stress-induced PT. Generally, both strain- and stress-induced PTs occur simultaneously at different places of the representative volume, leading to the necessity of developing a *fundamentally new theory for combined strain- and stress-induced PTs*, which considers strain rate and time effects, as well as evolving microstructure. Obtained results represent the first experimental findings in this direction.

Formal nanoscale [18,19] and microscale [32,33] phase-field approaches consider combined strain- and stress-induced PTs by studying coupled stress-induced dislocation evolution and phase transformations. However, they were not applied to and calibrated by any experimental data, and macroscale kinetics was not developed. Still, nucleation and growth stages are clearly seen in [18,19], in which growth in nanograined materials is promoted by small distance between different nuclei, their interaction and coalescence, neglected in the analytical approach [16,17]. Since pressure during time-resolved torsion with 1,000 RPM (3.5 GPa in BCC, 3.8 GPa in HCP, and averaged $p_{av} = 3.5$ GPa before torsion is practically equal to p_ϵ^d , growth is very slow. After torsion stops, pressure is higher (4.1 GPa in BCC and 4.5 GPa in HCP) but still close to p_ϵ^d , and the growth

takes few minutes. For torsion with 1,500 RPM, pressure is 3.45 GPa in BCC, 3.51 GPa in HCP, and $p_{av} = 3.45$ GPa before torsion, which even closer to p_{ε}^d . Actually, it is much below $p_h^r = 4.5$ GPa, and after plastic straining stops and shear stresses partially relaxed, pressure-induced reverse PT may occur within few minutes. After the reverse PT completes, $p_{av} = 3.9$ GPa, but without plastic straining, this does not cause direct PT.

Also, as follows from nanoscale phase-field simulations for a bicrystal [18,19] and microscale simulations for a polycrystal [31,32], steady high-pressure phase state obeys the PT condition

$$\langle \sigma_{ij} \rangle \varepsilon_t^{ij} = \Delta G^\theta, \quad (3)$$

where $\langle \sigma_{ij} \rangle$ and ε_t^{ij} are the averaged over polycrystal stress and transformation strain tensors, and ΔG^θ is the difference in the thermal part of the free energy between phases. This is the same condition as for stress-induced PTs. Since averaging filters out the internal stresses, steady phase state is governed by applied stress tensor or, in a simplified version, by applied pressure. The role of strain-induced contribution is to produce nucleation under low pressures, at which stress-induced nucleation is impossible. Plot in Fig. 3b is the first experimental confirmation of the prediction that the steady volume fraction is determined by pressure for combined strain-and stress-induced PT.

As follows from the theory and simulations on nucleation at the tip of dislocation pileup, stresses/pressure in the small nuclei of a high-pressure phase should be significantly larger than applied pressure (despite the volume reduction during PT), which was confirmed experimentally for PTs Si I-Si II and Si i-Si III [3]. This is not the case for Fe-7%Mn for small c (Figs. 1a and c and 2a and c), like that for α - ω PT in Zr [22]. If high-pressure phase consists of several martensitic variants, variant-variant transformations, representing often twinning, should lead to significant relaxation of deviatoric stresses during the PT. The maximum driving force for the PT is achieved at zero deviatoric stress after completing the PT in nuclei [34], which should reduce pressure in nuclei as well. For large c , pressure in the HCP phase is getting larger than in FCC phase, but this is due to higher yield strength of the HCP phase. At the same time, as is mentioned above, pressure in HCP phase is slightly larger than in BCC phase during torsion with 1,000 and 1,500 RPM, probably due to much shorter time for stress relaxation. While the same difference remains after torsion with 1,000 RPM, it may be related to increase in c by 0.3. Also, interesting result is obtained

that after 1500 RPM, the pressure in complete HCP phase at $r = 50 \mu\text{m}$ is 2.4 GPa higher than that at $r = 0 \mu\text{m}$ (Fig. 1a and c). This contradicts analytical solution in [16,17], which was a basis for the developing intuition for this process. However, more precise finite element method solutions [35,36,37] show a similar trend, which do not have any experimental confirmation till now.

Microstructure evolution

Obtained results in Fig. 4 for the microstructure evolution in the HCP phase leads to the new and very important rule:

Crystallite size of $\sim 30 \text{ nm}$, microstrain ~ 0.004 , and dislocation density $\rho_d = 1.1 \times 10^{15}/\text{m}^2$ in the HCP phase are steady during static compression and dynamic torsion, during and after the PT and after torsion and are independent of pressure, plastic strain tensor, its path, strain rates, and volume fraction of the HCP phase.

Indeed, during compression and torsion, stress-strain state of the sample is very heterogeneous and each material point undergoes completely different pressure, plastic strain tensor and its entire path [23,24,35,36,37]; that is why the same microstructure at different points of the sample and different stages of compression and torsion and PT means its independence of pressure, plastic strain tensor and its entire path and volume fraction of the HCP phase. The same microstructure for static compression and torsion with different rotation rates implies it is independence of the plastic strain rate. The maximum averaged strain rate for which data was collected, and this rule is valid, is $\dot{\gamma} = \omega r/h$, where γ is the shear strain during torsion, ω is the angular velocity, with maximum value of $\omega = 2\pi \times 1,500/60 = 157.1 \text{ /s}$, $r = 120 \mu\text{m}$, and the measured thickness $h = 9 \mu\text{m}$, resulting in $\dot{\gamma} = 2,094/\text{s}$.

Let us compare our results with the previous ones. Steady grain size and dislocation density and its independence of the radius and initial state during slow HPT with SPD was known for various materials [4,6,38-42]. Pressure independence of the steady grain size and/or dislocation density and/or hardness after HPT is found in [43]; their independence of the strain rate in the range from 0.004 to 20 /s was determined in [25]. All these results were obtained for a single-phase state after pressure release and ex situ measurements rather than in situ; it is known that during unloading, the grain size and dislocation density may change by a factor of 2 [44,45]. Also, during torsion

alone, plastic strain path is strongly shear-dominated and does not vary essentially. In situ studies on ω -Zr under static compression in DAC demonstrated independence of the steady crystallite size and dislocation density of pressure, plastic strain tensor, its path [26], with strong variation of the straining paths [23,24]. During the $\alpha \rightarrow \omega$ PT in Zr, the crystallite size and dislocation density in both phases strongly depends on the volume fraction of phases [27]. Here, results are obtained in situ in a broad strain rate range, from 0 for static compression to 2,094/s, broad range of straining paths during compression and torsion, during and after the PT.

Reduction in the crystallite phase of the BCC phase during compression before and during the PT in Figs. 2b and d is not surprising. However, results in Figs. 4b and c look nontrivial. Indeed, for 1,000 RPM, crystallite size varies non-monotonously in the narrow range 148-163 nm during torsion and then reduces strongly to 91 nm at constant load, while for 1,500 RPM, crystallite size almost monotonously reduces from 106 nm to a steady ~ 82 nm during torsion and slightly reduces to 69 nm at constant load. The potential reason may be in very different c for these cases.

Concluding Remarks

To summarize, the first experiments in dRDAC on SPD, BCC \leftrightarrow HCP PT, and microstructure evolution at pressure up to 27.6 GPa, rotation rates up to 1,500 RPM, and strain rates up to 2,094/s are performed with Fe-7%Mn alloy as an example. Real time data along the sample diameter with the time step of 5 ms and the beam spot of $1.3 \mu\text{m} \times 1.9 \mu\text{m}$ are collected. It was found for the PT start pressures that for the strain-induced PT, $p_{\epsilon}^d = 3.20$ GPa and $p_{\epsilon}^r = 6.05$ GPa for direct and reverse PTs, respectively; for the pressure-induced PT, $p_h^d = 11.4$ GPa and $p_h^r = 4.5$ GPa. Such a strong effect of plastic straining leads to simultaneous occurrence of the direct and reverse PTs in the pressure range $3.20 \text{ GPa} < p < 6.05 \text{ GPa}$. This results in a unique strain-controlled kinetic Eq. (1) with a stationary solution (2), which was not studied for any material. Here, material parameters in the kinetics for the strain-induced direct-reverse PTs and stationary volume fraction versus pressure are found for quasi-static loading.

During torsion with 1,000 and 1,500 RPM at low pressure close to p_{ϵ}^d , volume fraction of the HCP phase does not change. However, after torsion stops, it surprisingly increases by 30% within a few minutes after 1,000 RPM and HCP phase disappears after 1,500 RPM. These findings contradict general wisdom that strain-induced PTs occur only during straining, time is not a governing parameter, and kinetics is determined by plastic strain instead of time. Thus, nuclei of

the HCP phase are generated during straining at high strain rate, but growth/disappearance occur under stresses at a few minutes time scale. Consequently, a new theory of combined strain- and stress-induced PTs is required. Our nanoscale and microscale phase-field approaches bicrystal [18,19,32,33] could be a good starting point for such a theory at these scales and govern developing of the macroscale kinetics, which should generalize Eq. (1) significantly. Note that with increasing pressures, the PT time reduces, and we expect to detect essential evolution of the volume fraction of phases in real time, like for microstructure in Fig. 4c.

The following important rule for microstructure evolution is discovered: crystallite size of ~ 30 nm, microstrain ~ 0.004 , and dislocation density $\sim 1.1 \times 10^{15}/\text{m}^2$ in the HCP phase are steady during static compression and dynamic torsion, during and after the PT and after torsion. These parameters are independent of pressure, plastic strain tensor, its path, strain rates, and volume fraction of the HCP phase.

Obtained results open fundamental research on combined strain- and stress-induced PTs and microstructure evolution under dynamic SPD and high pressure in dRDAC for various material systems. This also possesses a significant applied potential for understanding and controlling processes in modern technologies and nature.

Acknowledgements

VIL acknowledges ARO (W911NF2420145), NSF (DMR-2246991 and CMMI-2519764), and Iowa State University (Murray Harpole Chair in Engineering). This work is performed at HPCAT (Sector 16), Advanced Photon Source (APS), and Argonne National Laboratory. HPCAT operations are supported by DOE-NNSA's Office of Experimental Science. The Advanced Photon Source is a U.S. Department of Energy (DOE) Office of Science User Facility operated for the DOE Office of Science by Argonne National Laboratory under Contract No. DE-AC02-06CH11357.

References

- 1 Bridgman P. W. Effect of high shear stress combined with high hydrostatic pressure. *Physical Review* 1935; 48: 825-847.
- 2 Blank V. D. & Estrin, E. I. Phase transitions in solids under high pressure. (Crc Press, 2013).

- 3 Yesudhas S, Levitas V. I, Lin F, Pandey K. K, Smith J. Unusual plastic strain-induced phase transformation phenomena in silicon. *Nature Communications* 2024; 15: 7054.
- 4 Edalati K, Bachmaier A, Beloshenko V. A, Beygelzimer Y, Blank V. D, Botta W. J, et al. Nanomaterials by severe plastic deformation: review of historical developments and recent advances. *Materials Research Letters* 2022; 10: 163-256.
- 5 Gao Y, Ma Y, An Q, Levitas V. I, Zhang Y, Feng B, Chaudhuri J, Williams A. G III. Shear driven formation of nano-diamonds at sub-gigapascals and 300 K. *Carbon* 2019; 146: 364-368.
- 6 Edalati K, Ahmed A. Q, Akrami S, Ameyama K, Aptukov V, Asfandiyarov RN, Ashida M, Astanin V, Bachmaier A, Beloshenko V, et al. Severe plastic deformation for producing superfunctional ultrafine-grained and heterostructured materials: an interdisciplinary review. *Journal of Alloys and Compounds* 2024; 1002: 174667.
- 7 Edalati K, Hidalgo-Jiménez J, Nguyen T. T, Sena H, Enikeev N, Rogl G, Levitas V. I, Horita Z, Zehetbauer M. J, Valiev R. Z, Langdon T. G. Severe plastic deformation of ceramics by high-pressure torsion: review of principles and applications. *Annual Review of Materials Research* 2025; 55: 89-124.
- 8 Patten J. A, Cherukuri H, Yan J. Ductile-regime machining of semiconductors and ceramics. In: Gogotsi Y, Domnich V, editors. *High Pressure Surface Science and Engineering*, Section 6. Bristol: Institute of Physics; 2004. p. 521-540.
- 9 Goel S, Luo X, Agrawal A, Reuben R. L. Diamond machining of silicon: a review of advances in molecular dynamics simulation. *International Journal of Machine Tool and Manufacture* 2015; 88: 131-164.
- 10 Lloyd J. T, Field D. M., Magagnosc D. J., Limmer K. R., Turnage S. A., Williams C. L., Clayton J. D. Manipulating shock waves with metallurgy. *Acta Materialia* 2022; 234: 118042.
- 11 Green H. W II, Burnley P. C. A new, self-organizing mechanism for deep-focus earthquakes. *Nature* 1989; 341: 733-737.
- 12 Levitas V. I. Resolving puzzles of the phase-transformation-based mechanism of the strong deep-focus earthquake. *Nature Communications* 2022; 13: 6291.
- 13 Levitas V. I. High-pressure phase transformations under severe plastic deformation by torsion in rotational anvils. *Materials Transactions* 2019; 60: 1294-1301.

- 14 Levitas V. I. Recent in situ experimental and theoretical advances in severe plastic deformations, strain-induced phase transformations, and microstructure evolution under high pressure. *Materials Transactions* 2023; 64: 1866-1878.
- 15 Levitas V. I. Severe plastic deformations, mechanochemistry, and microstructure evolution under high pressure: In Situ Experiments, Four-Scale Theory, New Phenomena, and Rules. 2025, 162 pages, <http://arxiv.org/abs/2508.14721>. *Progress in Materials Science*, 2026, accepted.
- 16 Levitas V. I. High pressure mechanochemistry: conceptual multiscale theory and interpretation of experiments. *Physical Review B* 2004; 70: 184118.
- 17 Levitas V. I. Continuum mechanical fundamentals of mechanochemistry. In: Gogotsi Y, Domnich V, editors. *High Pressure Surface Science and Engineering, Section 3*. Bristol and Philadelphia: Institute of Physics; 2004. p. 159-292.
- 18 Levitas, V. I, Javanbakht M. Phase transformations in nanograin materials under high pressure and plastic shear: nanoscale mechanisms. *Nanoscale* 2014; 6: 162-166.
- 19 Javanbakht, M, Levitas V. I. Phase field simulations of plastic strain-induced phase transformations under high pressure and large shear. *Physical Review B* 2016; 94: 214104.
- 20 Chen H, Levitas V. I, Xiong L. Amorphization induced by 60° shuffle dislocation pileup against different grain boundaries in silicon bicrystal under shear. *Acta Materialia* 2019; 179: 287-295.
- 21 Peng Y, Ji R, Phan T, Capolungo L, Levitas V. I, Xiong L. Effect of a micro-scale dislocation pileup on the atomic-scale multi-variant phase transformation and twinning. *Computational Materials Science* 2023; 230: 112508.
- 22 Pandey K. K, Levitas V. I. In situ quantitative study of plastic strain-induced phase transformations under high pressure: example for ultra-pure Zr. *Acta Materialia* 2020; 196: 338-346.
- 23 Levitas V. I, Dhar A, Pandey K. K. Tensorial stress-plastic strain fields in α - ω Zr mixture, transformation kinetics, and friction in diamond anvil cell. *Nature Communications* 2023; 14: 5955.

- 24 Dhar A, Levitas V. I, Pandey K. K, Park C, Somayazulu M, Velisavljevic N. Quantitative kinetic rules for plastic strain-induced α - ω phase transformation in Zr under high pressure. *NPJ Computational Materials* 2024; 10: 290.
- 25 Lin F, Levitas V. I, Pandey K. K, Yesudhas S, Park C. In-situ study of rules of nanostructure evolution, severe plastic deformations, and friction under high pressure. *Materials Research Letters* 2023; 11: 757-763.
- 26 Lin F, Levitas V. I, Pandey K. K, Yesudhas S, Park C. Rules for the crystallite size and dislocation density evolution in phases during α - ω transformation in Zr under high-pressure and severe plastic flow. *Acta Materialia* 2025; 295: 121151.
- 27 Edalati K, Wang Q, Enikeev N. A, Peters L-J, Zehetbauer MJ, Schafner E. Significance of strain rate in severe plastic deformation on steady-state microstructure and strength. *Materials Science and Engineering: A* 2022; 859: 144231.
- 28 Prescher, C, Prakapenka V. B. DIOPTAS: a program for reduction of two-dimensional X-ray diffraction data and data exploration. *High Pressure Research* 2015; 35: 223–230.
- 29 Lutterotti L, Matthies S, Wenk H. R, Schultz A. S, Richardson Jr J. W. Combined texture and structure analysis of deformed limestone from time-of-flight neutron diffraction spectra. *Journal of Applied Physics* 1997; 81: 594-600.
- 30 Ma Y, Selvi E, Levitas V. I, Hashemi J. Effect of shear strain on the $\alpha - \epsilon$ phase transition of iron: a new approach in the rotational diamond anvil cell. *Journal of Physics: Condensed Matter* 2006; 18: S1075-S1082.
- 31 Singh A, Jain A, Liermann H. P, Saxena S. K. Strength of iron under pressure up to 55 GPa from X-ray diffraction line-width analysis. *Journal of Physics and Chemistry of Solids* 2006; 67: 2197-2202.
- 32 Levitas V. I, Esfahani S. E, Ghamarian I. Scale-free modeling of coupled evolution of discrete dislocation bands and multivariant martensitic microstructure. *Physical Review Letters* 2018; 121: 205701.
- 33 Esfahani S. E, Ghamarian I, Levitas V. I. Strain-induced multivariant martensitic transformations: a scale-independent simulation of interaction between localized shear bands and microstructure. *Acta Materialia* 2020; 196: 430-433.
- 34 Levitas V. I, Stein E. Simple micromechanical model of thermoelastic martensitic transformations. *Mechanics Research Communications* 1997; 24: 309-318.

- 35 Levitas V. I, Zarechnyy O. M. Modeling and simulation of strain-induced phase transformations under compression in a diamond anvil cell. *Physical Review B* 2010; 82: 174123.
- 36 Levitas V. I, Zarechnyy O. M. Modeling and simulation of strain-induced phase transformations under compression and torsion in a rotational diamond anvil cell. *Physical Review B* 2010; 82: 174124.
- 37 Feng B, Levitas V. I, Kamrani M. Coupled strain-induced alpha to omega phase transformation and plastic flow in zirconium under high pressure torsion in a rotational diamond anvil cell. *Mat Sci Eng A A* 2018; 731: 623-633.
- 38 Valiev R. Z, Islamgaliev R. K, Alexandrov I. V. Bulk nanostructured materials from severe plastic deformation. *Progress in Materials Science* 2000; 45: 103-189.
- 39 Zhilyaev A. P, Langdon T. G. Using high-pressure torsion for metal processing: Fundamentals and applications. *Progress in Materials Science* 2008; 53: 893-979.
- 40 Pippin R, Scheriau S, Taylor A, Hafok M, Hohenwarter A, Bachmaier A. Saturation of fragmentation during severe plastic deformation. *Annual Review of Materials Research* 2010; 40: 319-343.
- 41 Valiev R. Z, Estrin Y, Horita Z, Langdon T. G, Zehetbauer M. J, Zhu Y. Producing bulk ultrafine-grained materials by severe plastic deformation: ten years later. *JOM* 2016; 68: 1216-1226.
- 42 Kerber M. B, Spieckermann F, Schuster R, von Baeckmann C, Fischer T, Schell N, Waitz T, Schafler E. In situ synchrotron X-ray diffraction during high-pressure torsion deformation of Ni and NiTi. *Advanced Engineering Materials* 2021; 23: 2100159.
- 43 Pandey K. K, Levitas V. I, Park C, Shen G. In situ study of microstructure evolution and $\alpha \rightarrow \omega$ phase transition in annealed and pre-deformed Zr under hydrostatic loading. *Journal of Applied Physics* 2024; 136: 115901.
- 44 Cao Y, Ni S, Liao X, Song M, Zhu Y. Structural evolutions of metallic materials processed by severe plastic deformation. *Materials Science and Engineering: R: Reports* 2018; 133: 1-59.
- 45 Edalati K, Horita Z. Universal plot for hardness variation in pure metals processed by high-pressure torsion. *Materials Transactions* 2010; 51: 1051-1054.